Composite Structures 326 (2023) 117599

Contents lists available at ScienceDirect

Composite Structures

journal homepage: www.elsevier.com/locate/compstruct

Assembling feather-like reentrant structures with multiple mechanical properties fabricated by laser powder bed fusion

Ruiyao Liu [a], Guofeng Yao [a], Jian Zhang [b], Yanan Yang [b], Zezhou Xu [b,*], Yuting Liu [b], Zhenglei Yu [b,*], Liang ping [b,*], Zhihui Zhang [b], Lei Dong [c], Chunyang Han [d]

[a] Department of Mechanics, School of Mechanical and Aerospace Engineering, Jilin University, Changchun 130022, China
[b] Key Lab of Bionic Engineering, Ministry of Education, Jilin University, Changchun 130022, China
[c] FAW Mould Manufacturing Co., Ltd., Changchun 130022, China
[d] Changchun Institute of Optics, Fine Mechanics and Physics, Chinese Academy of Sciences, Changchun 130022, China

ARTICLE INFO

Keywords:
Bio-inspired structure
Structural assembly
Euler theory
Steady thermal conduction
Energy dissipation effect

ABSTRACT

A new assembly design method for structural components is proposed. Inspired by the feathers of the grey crane, which have an energy dissipation effect, novel re-entrant scapus component and novel re-entrant double-crank component are proposed. Novel re-entrant structures are formed by assembling honeycomb structure (HS), poisson structure (PS), and chiral structure (CS). Laser powder bed fusion technology (LPBF) is utilized for the manufacturing of bio-inspired structures. And the impact of structural assembly on mechanical performance is comprehensively analyzed through experimental, numerical, and theoretical approaches. Euler theory is employed to predict the influence of bionic components on structural load trends, while explaining the relationship between compression load and deformation. Specifically, the average load capacity of bio-inspired scapus re-entrant structures and double-crank re-entrant structures exceeds that of their original designs by at least 55% and 13.2%, respectively. Moreover, specific energy absorption increases by a minimum of 8.6% and 3.4%, accompanied by improved heat dissipation performance in these structures. Finally, battery pack impact resistance models as well as thermal conductivity models for electric-powered vehicles are presented as examples to validate the potential application prospects of this novel bio-inspired re-entrant structure in engineering.

1. Introduction

Nature has always served as a wellspring of inspiration for humanity, offering strategic insights for human design. Countless bio-inspired structures with exceptional properties have emerged, bestowing immense potential for scientific exploration [1–3]. Emulating practical organisms found in nature to engineer functional structures holds remarkable significance. Over the past few decades, bio-inspired design has played a pivotal role in engineering disciplines. Porous structures are widely employed across various engineering applications owing to their outstanding energy absorption capabilities, lightweight composition, and superior strength. These applications encompass but are not limited to automotive [4,5], marine engineering [6], and aerospace sectors [7,8].

With the aid of experiments [9,10], theoretical research [11], and simulations [12,13], the bio-inspired porous structures under different conditions have been scientifically analyzed. While considering the structural protection performance, researchers also consider the structural role in various scenarios, such as thermal dissipation, magnetic isolation, vibration control, and so on. Meran et al. [14] used a combination of finite element methods and experiments to study the crash-resistance performance of aluminum hexagonal honeycomb structures with structural wall expansion angle, impact speed, and mass change. To explore the multifunctional application potential of functionally graded materials, Hohe et al. [15] experimentally and numerically designed multifunctional graded porous materials for aerospace applications and optimized their properties to achieve the needed performance in applications. Inspired by the excellent mechanical properties of cuttlefish porous bone tissue in resisting high hydrostatic pressure in the deep sea, Mao et al. [16] studied 3D-printed honeycomb materials with high mechanical properties. This research shows that bio-inspired structures have stronger strength and energy absorption than common lattices, conventional polymers, and metal foams.

There are various high-quality biological structures in nature, among

* Corresponding authors.
E-mail addresses: zzxu20@mails.jlu.edu.cn (Z. Xu), zlyu@jlu.edu.cn (Z. Yu), Liangping@jlu.edu.cn (L. ping).

https://doi.org/10.1016/j.compstruct.2023.117599
Received 5 June 2023; Received in revised form 30 August 2023; Accepted 3 October 2023
Available online 5 October 2023

which the various functional capacities of feathers have been recognized by scientists around the world [17–19]. Feathers possess exceptional mechanical properties, including their lightweight nature, remarkable bending resistance, and efficient energy absorption capabilities. These properties have attracted the attention of researchers. Bio-inspired structures inspired by bird feathers are increasingly becoming a leader in the engineering field. Sharma et al. [20] designed novel crack propagation structures inspired by the rachis pattern of bird feathers, which opened a new way toward the development of advanced functional materials with adjustable and failure-proof designs. Sharma et al. [21] conducted an investigation into the manufacturing structure of fuses using both experimental and numerical methods, analyzing the impact of thickness, shape, and loading direction on the structure's performance under uniaxial compression and three-point bending. The study found that the bio-inspired design of bird feathers exhibited significantly better compression performance.

Due to the complexity of bio-inspired structures, traditional manufacturing methods cannot manufacture bio-inspired components [22,23]. With the development of additive manufacturing technology, additive manufacturing technology has accurately realized complex component manufacturing. Inspired by the natural ultralight structure, Pelanconi et al. [24] designed a periodic minimal surface structure to optimize the stiffness and density under bending load and studied its optimal performance in terms of stiffness and density by stereo lithography printing. Additive manufacturing has effectively expanded the design and application of novel lattice structures. Du et al. [25] conducted a study on a novel 3D-printed lattice structure inspired by the beetle front wing, investigating the impact of 3D-printing process parameters on densification behavior, microstructure, and mechanical properties. Similarly, Pasquale et al. [26] utilized laser fusion 3D printing (SLM) to analyze the influence of the 3D printing process on the mechanical properties of biomimetic porous materials.

Inspired by the energy dissipation effect of grey crane feathers, novel bio-inspired re-entrant components with exceptional energy dissipation performance are designed. These components are assembled into various forms of re-entrant structures: Scapus Honeycomb Structure (PHS), Double-crank Honeycomb Structure (DHS), Scapus Poisson Structure (PPS), Double-crank Poisson Structure (DPS), Scapus Chiral Structure (PCS), and Double-crank Chiral Structure (DCS). Experimental samples using LPBF have been conducted to manufacture these bionic structures. Numerical simulations and theoretical analysis have been employed to assist in the evaluation of their structural performance. The novel design, inspired by biological structures, has demonstrated significant improvements in both crashworthiness and thermal dissipation capabilities. Structural assembly holds great potential for enhancing mechanical performance and enabling future engineering applications.

2. Bionic re-entrant structures' assembly

2.1. Structural assembly

The structural configuration of the gray crane feather endows it with great elasticity and flexibility, allowing it to absorb external impact and reduce damage. It demonstrates excellent lightweight and impact protection capabilities. This can be explained by the unique structure of the rachis and barbs in the gray crane feather [24], as shown in Fig. 1. The microscopic images of gray crane feathers showcase its intricate structure and texture, revealing the unique features that provide excellent flight performance and adaptation to the environment, as shown in Fig. 1 (b) and (c). Firstly, the hollow and robust structure of the scapus allows the entire feather to withstand and disperse impact when subjected to external collisions, thereby reducing the occurrence of damage. This hollow configuration also enables the feather to remain lightweight, which is beneficial for the gray crane to minimize energy consumption during flight. Secondly, there exists a barb-like mechanism between the barbs in gray crane feathers, as shown in Fig. 1 (c). This type of connection provides both strength and flexibility to the feathers. The barb-like interlock extends from the center of the scapus to the edges of the feather. This arrangement and combination of barbs allow the feathers to better disperse external force and effectively reduce the damage caused by impacts. Additionally, within the feather, we can observe slender and curved fiber structures that connect with each other through small curved branches, as shown in Fig. 1 (b). The curved connections extend from the center to the edges of the feather, forming a complex network structure. This arrangement helps to reduce external impact forces, providing additional support and stability. These feathers, with outstanding flexibility and strength, allow the gray crane to withstand vibrations and external forces during flight.

By drawing inspiration from the structural features of the crane feather, novel re-entrant scapus structures and bio-inspired re-entrant double-crank structures are proposed, as shown in Fig. 1 (d) and (e). The design is inspired by the scapus of the feather and double-crank connection of gray crane barbs, which are mirrored and reconnected to create structurally unique and functional components. In the design process of these novel structures, traditional honeycomb structure, negative poisson structure, and chiral structure are referenced. By combining these traditional structures with the characteristics of crane feathers, novel bio-inspired structures are successfully designed. The structural dimensions of these components are shown in Fig. 2. In the field of engineering, these innovative reentrant components can be

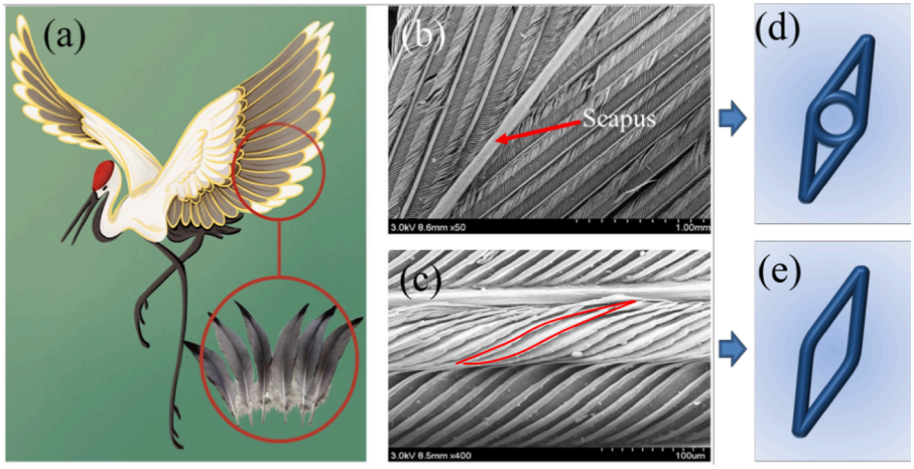

Fig. 1. The grey crane feathers' inspiration. (a) The grey crane and its feathers; (b) Partial magnification of the gray crane feather (including the scapus); (c) Electron microscopy of hyperbolic arrangement. (d) The re-entrant scapus component. (e) The re-entrant double-crank component.

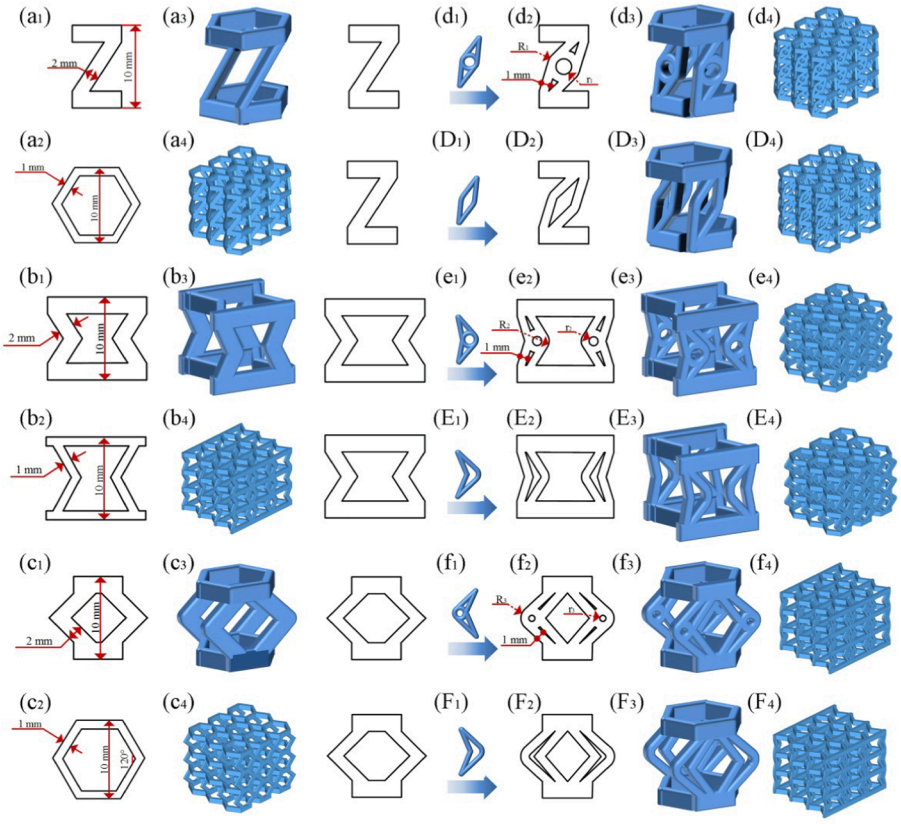

Fig. 2. Bio-inspired structures; (a_1) The Z section and the vertical section size of CS; (a_2) The top view section of CS; (a_3) The chiral unit; (a_4) CS; (b_1) The vertical section of PS; (b_2) The top view section of PS; (b_3) The negative poisson unit; (b_4) PS; (c_1) The vertical section of HS; (c_2) The top view section of HS; (c_3) The honeycomb unit; (c_4) HS; (d_1) The scapus re-entrant chiral component; (d_2) The Z section and the vertical section size of PCS; (d_3) The scapus chiral unit (d_4) PCS; (D_1) The double-crank re-entrant chiral component; (D_2) The vertical section of DCS; (D_3) The double-crank chiral unit; (D_4) DCS; (e_1) The scapus re-entrant negative poisson component; (e_2) The vertical section of PPS; (e_3) The scapus negative poisson structure; (e_4) PPS; (E_1) The double-crank re-entrant negative poisson component; (E_2) The vertical section of DPS; (E_3) The double-crank negative poisson unit; (E_4) DPS; (f_1) The scapus re-entrant honeycomb component; (f_2) The vertical section of PHS; (f_3) The scapus honeycomb unit; (f_4) PHS (F_1) The double-crank re-entrant honeycomb component; (F_2) The vertical section of DHS; (F_3) The double-crank honeycomb unit; (F_4) DHS. $R_1 = 2$ mm; $r_1 = 1$ mm; $R_2 = 1.5$ mm; $r_2 = 0.5$ mm; $R_3 = 1.375$ mm; $r_3 = 0.375$ mm.

applied to lightweight design, structural optimization, and other aspects, providing more reliable and efficient solutions for engineering projects.

2.2. Material properties analysis

The bio-inspired structures are prepared by using the laser powder bed fusion (LPBF) equipment FS403P and polymers (nylon). The SLS process is performed under argon protection to ensure that the oxygen content is below 300 ppm. XRD characterization at room temperature (~298.15 K) reveals that the powder composition is solely Nylon phase with no other secondary phases observed, as evidenced in Fig. 3 (b). Solvent precipitation is used to prepare Nylon powder, with a particle size range between 10 ~ 100 μm, as depicted in Fig. 3 (c). The microstructure of Nylon powder, displayed in Fig. 3 (d), reveals that most of the powder particles take on regular spherical shapes. Orthogonal stacking can occur on the powder bed, which involves composite stacking of large particle size powder and small particle size powder, leading to reduced porosity of the powder bed and improved quality of model form. However, the different 3D-printed parameters result in performance differences in the manufactured structures [27,2]8. This allows for a comparison of the differences in their structural mechanical properties. The 3D-printing parameters for LPBF are in Table 1.

Fig. 3 (e) shows scanning electron microscope (SEM) images of the structural surface morphology. The structural microstructure surface is rough. The reason is that the bonding between powder mainly depends upon the surface tension of the polymer melt in the process of sample forming, and the particles can flow freely in the forming process. Nylon powder presents a semi-molten state on the structural surface and sticks to the structural surface due to heating. It results in defects such as blocks and holes in the surface. It is also the reason why the mass of the 3D-printed sample is larger than the theoretical mass. The mass is shown in Fig. 3 (f).

The DT Series microcomputer control testing machine is utilized to obtain the tensile and compression curves of Nylon samples, as depicted in Fig. 4. The experiments are conducted uniaxially at a displacement rate of 1 mm/min. The density of the Nylon material is 1100 kg/m^3, while its elastic modulus and poisson ratio are 500 MPa and 0.38, respectively. Due to the different material reactions under different compression rates, Nylon material can be affected by the rate of deformation. For the structural impact testing in this study, aluminum alloy is chosen as the material because the aluminum alloy is not sensitive to strain rate [29], aluminum alloy 6063T6 is considered in structural impact models. The structural deformation modes and energy absorption capacity are comprehensively investigated. In this paper, the impacted thin-walled tube model is used to verify the parameters' correctness of aluminum alloy 6063T6. # Single Surface Contact is used for the contact between tube walls during the process of crushing. #Surface to Surface Contact is used to describe the contact between the thin-walled tube and the rigid wall. The coefficient of dynamic friction is 0.15, and the coefficient of static friction is 0.15 [30]. The length of the aluminum alloy square pipe is 200 mm, and the weight of the rigid wall

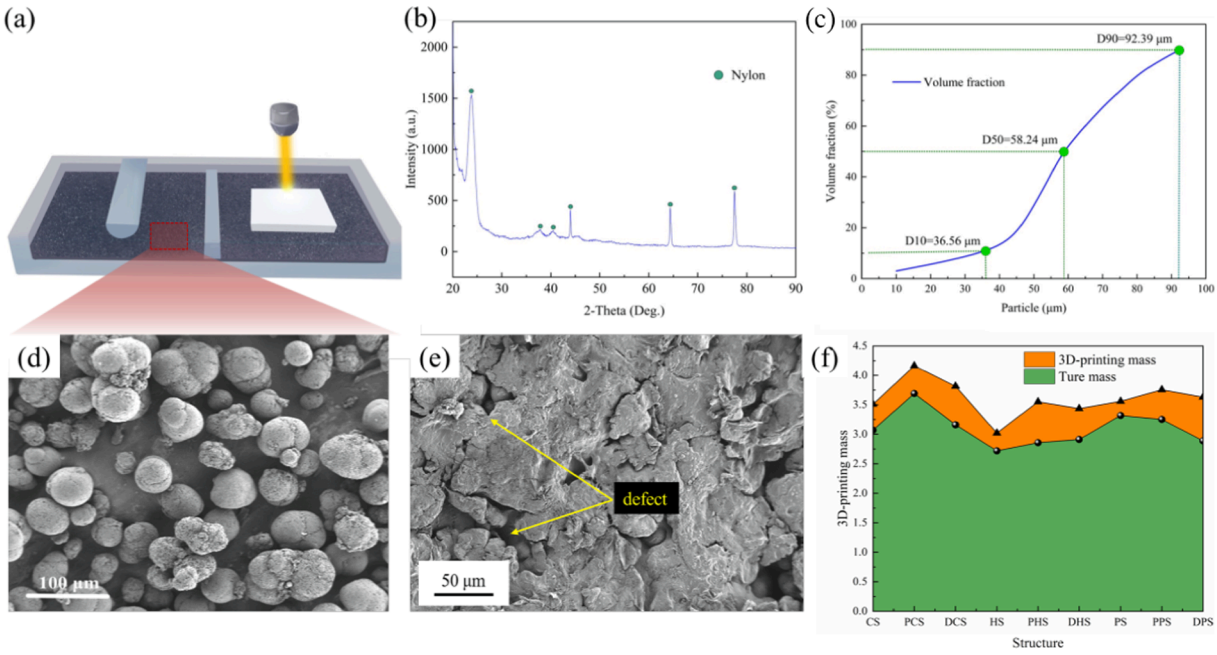

Fig. 3. Additive manufacturing process and material samples analysis. (a) SLS manufacturing process. (b) XRD curve of Nylon powder. (c) Cumulative distribution of Nylon powder size. (d) Microscopic morphology of Nylon powder. The performance verification of the aluminum alloy rectangular tube; (e) SEM image of the sample surface; (f) The mass comparison of the 3D printed samples, where the ture mass refers to the samples' mass derived from the calculation based on the material density, and the 3D-printing mass refers to the measured mass of samples after it is produced by additive manufacturing.

Table 1
3D-printing settings for FS403P.

Parameters	Scanning speed (mm/s)	Build cavity temperature (°C)	Laser power (W)	Preheating temperature (°C)	Jumping speed (mm/s)	Material
Tensile sample	7.62	169	22	140	2.54	PS300

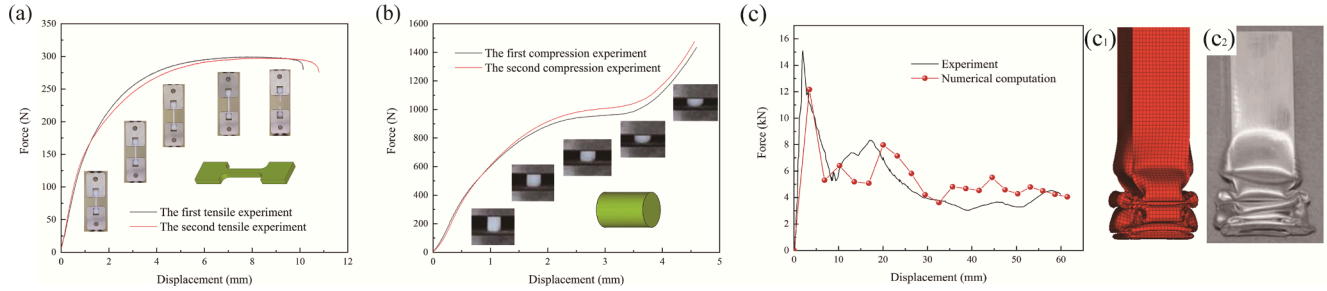

Fig. 4. Material performance; (a) The uniaxial tensile result of nylon; (b) The compression result of nylon; (c) The force–displacement verification of the aluminum alloy rectangular tube; The performance of the aluminum alloy rectangular tube; (c_1) The simulated deformation mode of the aluminum alloy rectangular tube; (c_2) The experimental deformation mode of the aluminum alloy rectangular tube [31]. The density of Aluminum alloy 6063T6 is 2700 kg/m^3. The elastic modulus is 68.2 GPa, and poisson ratio is 0.3 [31]. The dimensions of the tensile and compression samples are shown in the attachment of models.

is 40 kg. The initial velocity of the rigid wall is 7.02 m/s. Fig. 3 (c) shows that the numerical crushing result is in good agreement with the experimental results, especially in terms of force and the order of collapse modes (Fig. 4 ($c_{1\text{-}2}$)). Therefore, it can be considered that properties of aluminum alloy 6063T6 can well calculate the crashworthiness of aluminum alloy structures, as shown in Fig. 4.

3. Computational and theoretical models of biomimetic re-entrant structures

3.1. Performance analysis indicators

The evaluation criteria commonly employed for lattice structures comprise of plateau force (*F*), Energy Absorption (*EA*), and Specific Energy Absorption (*SEA*) [32]. These parameters are indicative of the lattice structure's crashworthiness and energy absorption potential.

F is the mean force during the compression process after reaching structure bending, as shown in Eq. (1). A higher mean force indicates better crashworthiness of the structure.

$$F = \frac{1}{x_0 - x_1}\int_{x_1}^{x_0} F\mathrm{d}x \tag{1}$$

EA, which stands for energy absorption, is a crucial factor in determining the protective capacity of a structure during the compression process. A higher *EA* value indicates a better ability to absorb energy and provide protection. It is important to note that *EA* refers to the energy absorption of the entire structure during compression, as demonstrated in Eq. (2).

$$EA = \int_{x=0}^{x=x_0} F\mathrm{d}x \tag{2}$$

SEA, *which* stands for structural energy absorption, is a crucial performance parameter for evaluating the effectiveness of structural protection and energy absorption. It is calculated as the amount of energy absorbed by a structure per unit mass during compression, as demonstrated by Eq. (3)..

$$SEA = \frac{EA}{M_{str}} \tag{3}$$

3.2. Compression theory models

Taking Fig. 5 (a) as an example. The structural wall undergoes local tension or bending when the structure is under linear elastic compression. The load is applied vertically to the structure, and there is no lateral load. The bending moment M of the structural wall is [34].

$$M = \frac{F_b l \sin\theta}{2} \tag{4}$$

where l is the length of the structural wall. t is the width of the structural wall. b is the thickness of the structural wall. S is the contact area of the compressed structure, $S = (l + h)b$, as shown in Fig. 5. At the same time, satisfy

$$F_b = \frac{\sigma_1 S}{2} \tag{5}$$

Structural size conforms to $t/l < 0.25$, which meets the slender rod

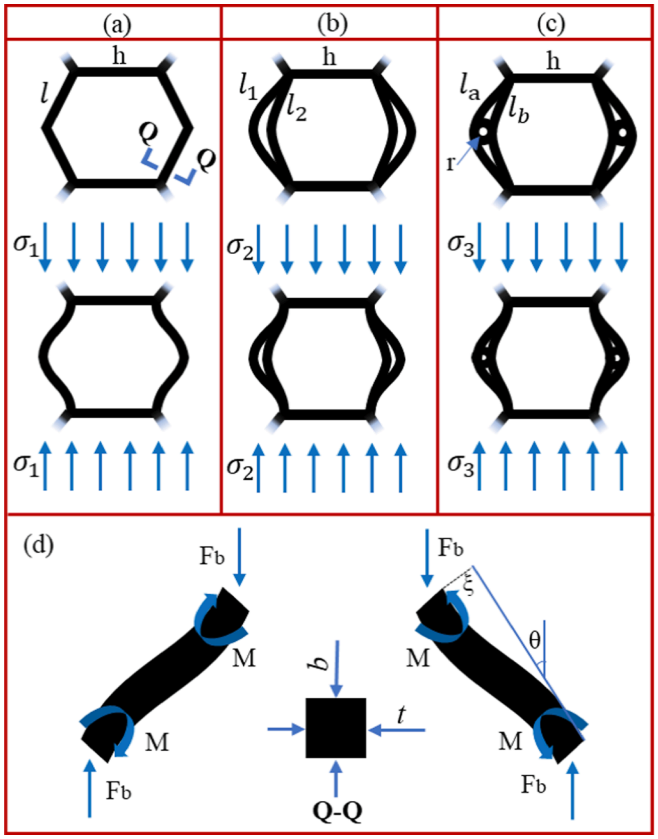

Fig. 5. Bio-inspired structures undergo linear elastic tension or bending caused by the bending-induced boundary deformation of the structure. (a) The original structure undergoing compressive deformation. (b) The double-crank re-entrant structure undergoing compressive deformation. (c) The scapus re-entrant structure undergoing compressive deformation. (d) The compressive load of the structure.

criterion [34]. According to the Euler theorem, obtain

$$\xi = \frac{F_b l^3 \sin\theta}{24 E_s I} \tag{6}$$

where Moment of inertia is $I = bt^3/12$. So the strain of the structure is

$$\varepsilon = \frac{\xi \sin\theta}{l\cos\theta} = \frac{\sigma_1 S l^2 \sin^2\theta}{24 E_s I \cos\theta} \tag{7}$$

The elastic modulus of the original structure is

$$\frac{E}{E_s} = \left(\frac{t}{l}\right)^3 \frac{\cos\theta}{2(h/l+1)\sin^2\theta} \tag{8}$$

Taking Fig. 5 (b) as an example. The structural wall undergoes local tension or bending when the structure is under linear elastic compression. The load is applied vertically to the structure, and there is no lateral load. The bending moment M of the structural wall is [34].

$$M = \frac{F_b l_1 \sin\theta}{4} \tag{9}$$

$S = (l_1 + l_2 + h)b$. satisfy

$$F_b = \frac{\sigma_1 S}{4} \tag{10}$$

So

$$\xi = \frac{F_b l_1^3 \sin\theta}{48 E_s I} \tag{11}$$

Therefore, structural strain is

$$\varepsilon = \frac{\xi \sin\theta}{l_1 \cos\theta} = \frac{\sigma_1 S l_1^2 \sin^2\theta}{48 E_s I \cos\theta} \tag{12}$$

So the elastic modulus of the double-crank re-entrant structure is

$$\frac{E}{E_s} = \left(\frac{t}{l_1}\right)^3 \frac{\cos\theta}{2(h/l_1 + l_2/l_1 + 1)\sin^2\theta} \tag{13}$$

Similarly, the elastic modulus of the scapus re-entrant structure is

$$\frac{E}{E_s} = \left(\frac{t}{l_a}\right)^3 \frac{\cos\theta}{2(h/l_a + l_b/l_a + \pi r/l_a + 1)\sin^2\theta} \tag{14}$$

3.3. Compression models

The explicit dynamics program Ls-Dyna is utilized to simulate both the quasi-static compression and impact of the bio-inspired structures. The bio-inspired structures, along with the upper and lower rigid plates, are depicted in Fig. 6 (a), with the total weight of the plates being 10.08 kg. The lower rigid plate is immobile and provides six degrees of freedom to support the bio-inspired structure, while the upper rigid plate moves downward continuously. During the dynamic compression process, Surface to Surface contact is employed to establish contact between the bio-inspired structure and the rigid plate, while Single Surface contact is utilized to ensure that the bio-inspired structures themselves do not interpenetrate. To prevent interpenetration, a friction coefficient of 0.15 [30] is set.

3.4. Steady thermal conduction models

During the operation of an electric vehicle, the battery maintains stable endurance and generates a relatively constant amount of heat. However, there is a structural demand for heat conduction to prevent battery loss caused by excessive temperature rise. Therefore, it is necessary to conduct a steady-state thermal conductivity analysis. The structural steady-state heat conduction model is shown in Fig. 6 (b). The heat exchanger is a sandwich structure composed of the 6063T6 bio-inspired sandwich and upper and lower panels with a length of 38

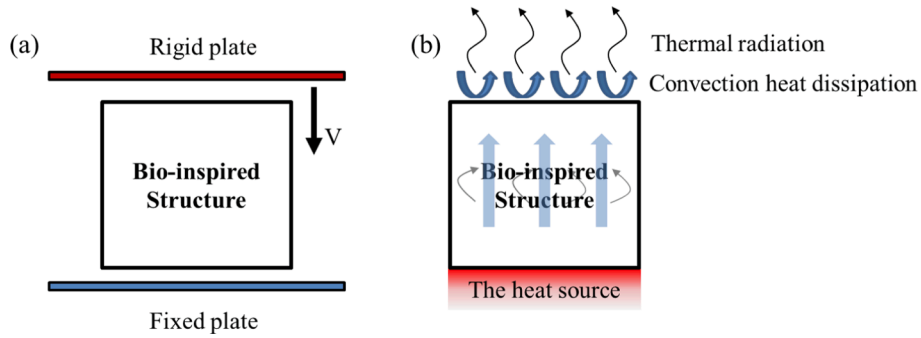

Fig. 6. Simulation models of the bio-inspired structures (a) Dynamic impact simulation model of the bio-inspired structure; (b) steady-state heat conduction simulation model of the bio-inspired structures.

mm, a width of 34 mm, and a thickness of 1 mm. The steady-state heat conduction of the bio-inspired structures is calculated by ANSYS Thermal. The principal equation of steady-state heat conduction is [33]

$$\boldsymbol{\lambda T} + \boldsymbol{B\dot{T}} = \boldsymbol{P} + \boldsymbol{N} \tag{16}$$

where $\boldsymbol{T}$ is the temperature matrix of the mesh node. $\dot{\boldsymbol{T}}$ is the temperature gradient matrix. $\boldsymbol{P}$ is the external heat flow vector. $\boldsymbol{N}$ is the nonlinear external heat flow vector dependent on temperature. $\boldsymbol{\lambda}$ is the thermal conductivity. $\boldsymbol{B}$ is the structural heat capacity matrix.

The convective heat coefficient is 5 W/(m^2 K) on both the upper and lower plate surfaces and the inner surface of the bio-inspired structures with the external environment. The surface temperature of the upper panel is 573.15 K. The initial temperature of the environment and the overall bio-inspired structures is 295.15 K. The four faces around the upper and lower panels of the bio-inspired structures are treated as adiabatic boundaries. The convective heat transfer surface of the bio-inspired structure is treated with thermal radiation at the same time. The surface emissivity is 1, and the heat transfer of the bio-inspired structure at 1 s is calculated.

3.5. The mesh-independence analysis

Because the mesh size of the simulation directly affects the computation efficiency and accuracy, the mesh-independent validation of 0.25 mm, 0.5 mm, 0.75 mm, and 1 mm is used for the bio-inspired units, as shown in attachment S1. Because the simulation result is equivalent to the structural deformation according to the given shape function, the stiffness of the simulation is larger than the conjectural solution. And the finer the mesh is, the closer it is to the conjectural solution. Then, when comparing the mesh independence, the mesh size of 0.15 mm is taken as the energy reference E_0 to conduct the mesh-independence analysis under different mesh sizes.

$$a_{\text{Error}} = \frac{E - E_0}{E_0} \times 100\% \tag{15}$$

where E is the energy absorption of structures with different mesh sizes. a_{Error} is the calculation error under different mesh sizes.

Fig. 7 shows the energy absorption errors under different mesh sizes when the structural unit is compressed by 3.4 mm. It can be found that the energy absorption error increases with the increase of the mesh size. When the models' mesh is less than 0.5 mm, the energy absorption error tends to be stable and the energy absorption error is less than 10 %. The influence on the mesh size change is negligible. To better balance the accuracy and the computation efficiency of the simulation, the mesh size is set to 0.5 mm.

4. Mechanical property analysis

4.1. Compression properties analysis

Fig. 8 shows the data results obtained from the quasi-static compression with a compressive speed of 1 mm/min. It can be seen from Fig. 8 (a_1) (a_2) (a_3) that the compressive force–displacement curves of the bio-inspired structures present three stages, namely the elastic deformation stage, stress softening stage, and platform stress stage. The theoretical, experimental, and simulation results have good similarity, reflecting the accuracy of the results. The similarity is up to 85 %. Most of the energy absorbed by the protection structures occurs during the platform stress stage [34]. Eq. (24), Eq. (25), and Eq. (26) are used to calculate F, EA, and SEA of the bio-inspired structures. And the results are shown in Fig. 8 (b) (c) (d). The results show that compared with CS, F of PCS and DCS increases by 72.2 % and 24.8 %, EA by 77.1 % and 23.3 %, and SEA by 48.2 % and 20 %, separately. Compared with HS, F of PHS and DHS increases by 52.7 % and 27.6 %, EA by 58.1 % and 23.7 %,

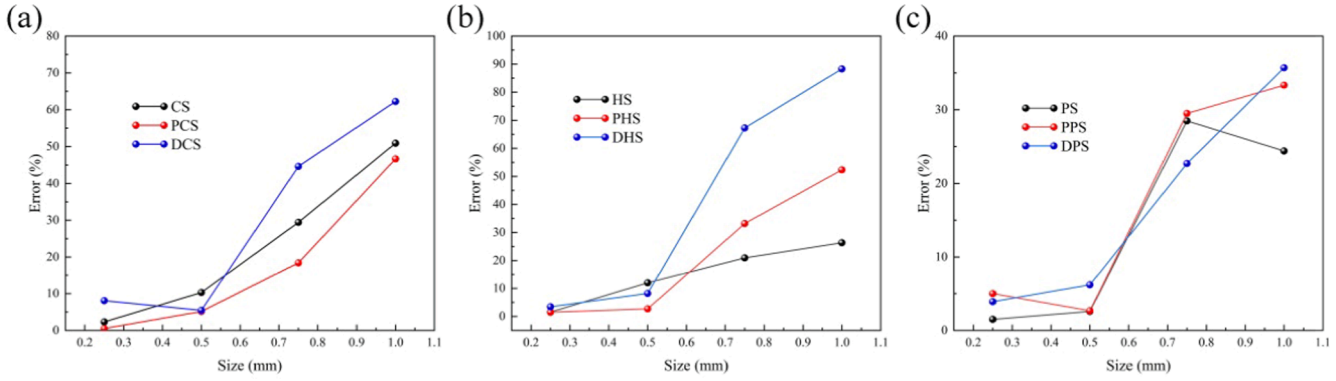

Fig. 7. Mesh independence verification; (a) Mesh independence verification of novel chiral units; (b) Mesh independence verification of novel honeycomb units; (c) Mesh independence verification of novel negative poisson units.

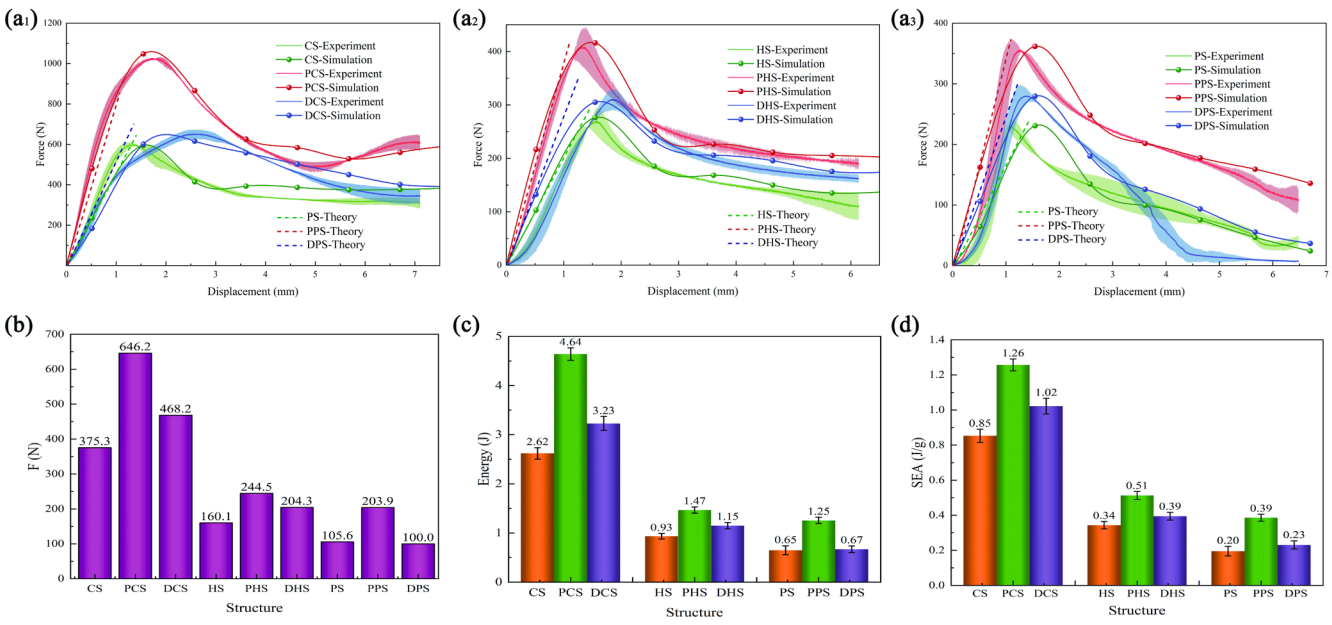

Fig. 8. Quasi-static compression results; (a_1) Compressive force–displacement curve of bio-inspired chiral structures; (a_2) Compressive force–displacement curve of bio-inspired honeycomb structures; (a_3) Compressive force–displacement curve of bio-inspired negative poisson structures; (b) F of bio-inspired structures; (c) EA of bio-inspired structures; (d) SEA of bio-inspired structures.

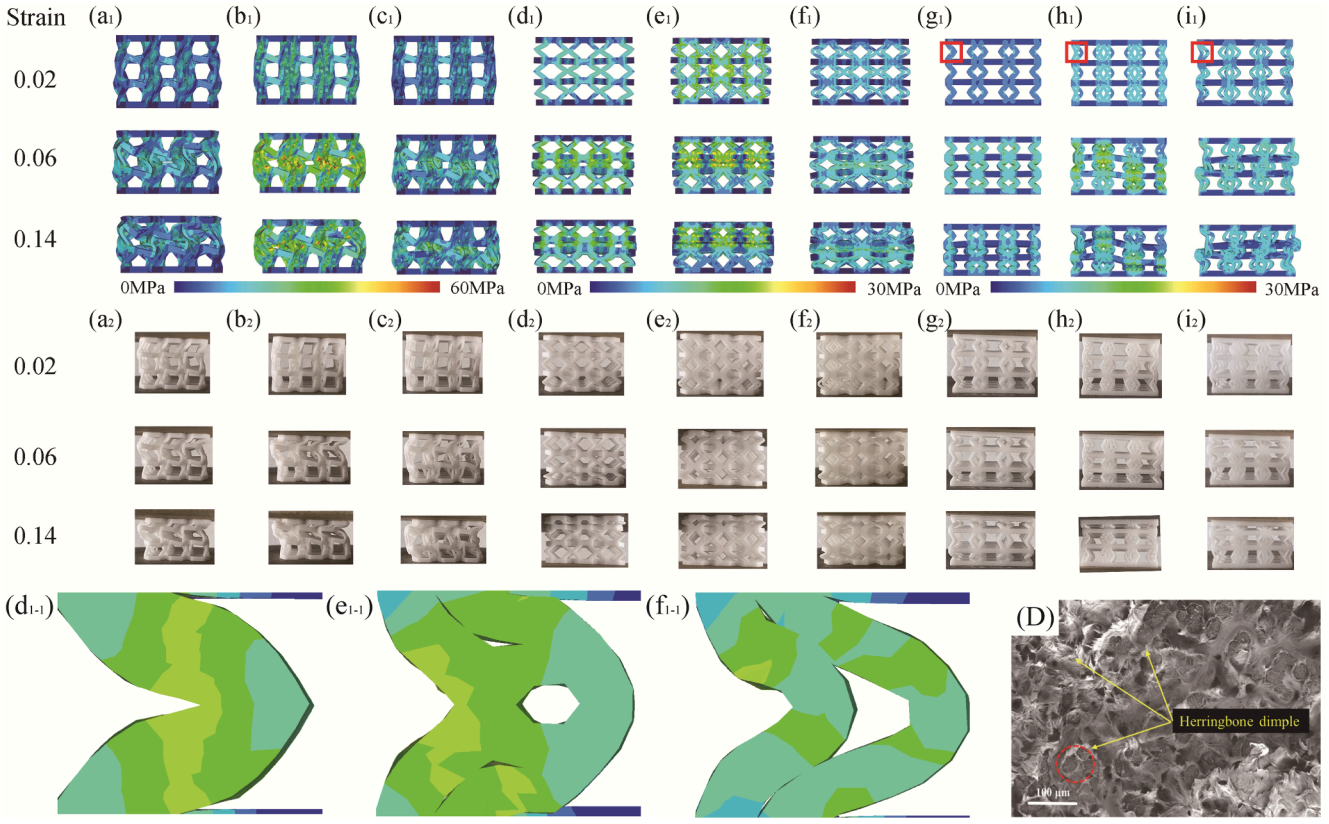

Fig. 9. Structural compression deformation; (a_1) CS simulation deformation; (a_2) CS experiment deformation; (b_1) PCS simulation deformation; (b_2) PCS experiment deformation; (c_1) DCS simulation deformation; (c_2) DCS experiment deformation; (d_1) HS simulation deformation; (d_2) HS experiment deformation; (e_1) PHS simulation deformation; (e_2) PHS experiment deformation; (f_1) DH S simulation deformation; (f_2) DHS experiment deformation; (g_1) PS simulation deformation; (g_2) PS experiment deformation; (h_1) PPS simulation deformation; (h_2) PPS experiment deformation; (i_1) DPS simulation deformation; (i_2) DPS experiment deformation. (g_1) The detail view of PS simulation deformation; (h_1) The detail view of PPS simulation deformation; (i_1) The detail view of DPS simulation deformation; (D) The fracture detail SEM figure of structures.

and SEA by 50 % and 14.7 %, separately. Compared with PS, F of PPS and DPS increases by 93.1 % and −5%, EA by 92.3 % and 3.1 %, and SEA by 95 % and 15 %, respectively. It shows that the novel bio-inspired re-entrant design method can effectively improve the protection performance of the lattice structures.

Fig. 9 (g) furthermore compares the compression deformation modes of the bio-inspired re-entrant structures (PCS, DCS, PHS, DHS, PPS, DPS) and the original structures (CS, HS, PS). The compressive strain is 002, 0.06, 0.14, and the deformation modes are similar, which moreover proves the accuracy of compression simulation. It is worth noting that HS and PS occur the overall transverse buckling during the compression, which leads to the failure of partial structures to fully dissipate energy. This is one of the reasons for the low-energy absorption effect of HS and PS. In contrast, the deformation energy absorption of the bio-inspired scapus structures is more stable during compression. The reason, why the energy absorption performance of the bio-inspired scapus structure and the bio-inspired double-crank structures is better than that of the original structures, is that the bio-inspired components generate more plastic energy absorption during the deformation.

With the deformation of the structure, micro-voids nucleate, grow, slip, and aggregate to form a ductile dimple fracture, as shown in Fig. 9 (D). In the ductile dimple at the compression fracture surface, the fiber direction is consistent and presents a distinct herringbone pattern. However, there are also some small ductile dimples with fibers torn in

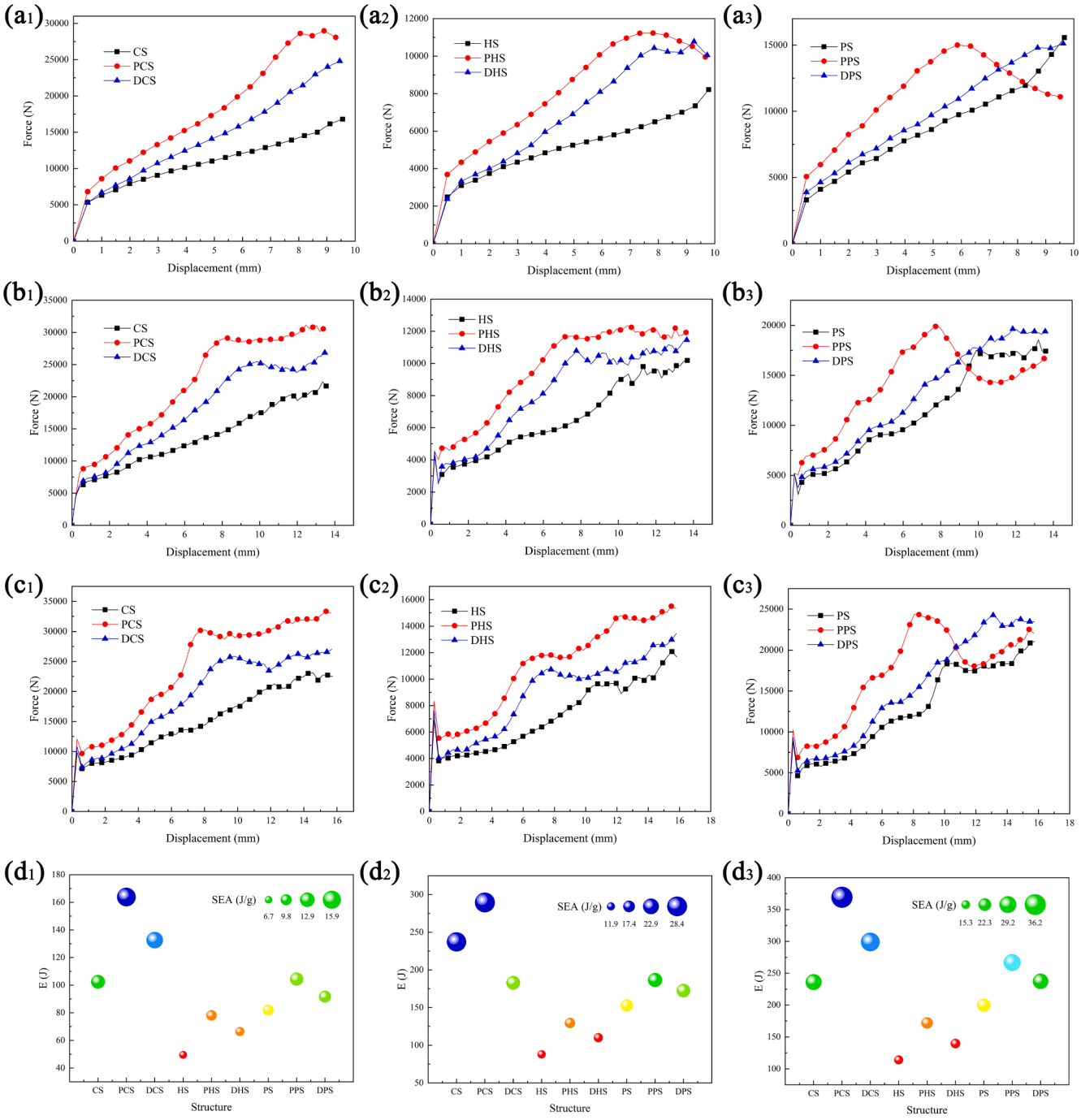

Fig. 10. ($a_{1\text{-}3}$) Structural impact results with initial velocity $V_0 = 10$ m/s ($b_{1\text{-}3}$) Structural impact results with initial velocity $V_0 = 20$ m/s ($c_{1\text{-}3}$) Structural impact results with initial velocity $V_0 = 30$ m/s (d_1) Structural energy absorption results with initial velocity $V_0 = 10$ m/s (d_2) Structural energy absorption results with initial velocity $V_0 = 20$ m/s (d_3) Structural energy absorption results with initial velocity $V_0 = 30$ m/s.

other directions, as shown in Fig. 9 (D). This indicates that the structural damage during compression mainly occurs through ductile fracture, and the fracture site is subjected to uniaxial bending load.

4.2. Shock properties analysis

In this section, the impact behaviors of bio-inspired re-entrant structures (PCS, DCS, PPS, DPS, PHS, DHS) and original structures (CS, PS, HS) at low ($V_0 = 10$ m/s), medium ($V_0 = 20$ m/s) and high ($V_0 = 30$ m/s) initial velocities are comparatively studied, including impact bearing capacity and energy absorption, as shown in Fig. 10. Based on the impact simulation model in Fig. 6 (a), dynamic impacts with initial velocities of 10 m/s, 20 m/s, and 30 m/s are carried out on the bio-inspired structures. And the influence of the bio-inspired re-entrant design on energy absorption is analyzed. Fig. 10(a_1) (b_1) (c_1) shows the force–displacement curves of CS, PCS, and DCS with initial velocities of 10 m/s, 20 m/s, and 30 m/s, individually. Fig. 10 (a_2) (b_2) (c_2) and Fig. 10 (a_3) (b_3) (c_3) show the force–displacement curves of HS, PHS, DHS, and PS, PPS, and DPS at initial velocities of 10 m/s, 20 m/s, and 30 m/s, individually. It can be seen that the anti-impact load of different bio-inspired structures increases with the increase of initial impact velocity. Under the same impact velocity, the impact load of the bio-inspired re-entrant scapus structure is significantly greater than that of the original structure, and the average bearing capacity is increased by more than 55 %. In terms of impact resistance and energy absorption of the bio-inspired structures, the energy absorption effect of the bio-inspired re-entrant structure PCS is better than that of other bio-inspired structures at low speed, medium speed, and high speed, all of which is 26.7 % higher than that of the traditional structures, as shown in Fig. 10 (d_1) (d_2) (d_3). In conclusion, the crashworthiness and energy absorption capacity of the lattice structure can be improved by the re-entrant scapus component.

Fig. 11 compares the deformation modes of bio-inspired structures at different initial impact velocities. In the process of impact compression, bio-inspired chiral structures all show a global deformation mode (torsional energy absorption), and the stress distribution is relatively uniform. However, other bio-inspired structures show a gradual deformation mode (vertical energy absorption deformation), and the stress is mainly concentrated in the vertical connection parts. Finally, the bio-inspired structures enter the densification stage with the increase of compression. An interesting phenomenon can be obeyed from deformation modes. After the bio-inspired re-entrant scapus structure is impacted, the structural re-entrant support components undergo morphologic changes such as bending or torsion. Due to such morphological changes in the re-entrant structural components, the re-entrant components contact the upper and lower parts to support the upper and lower parts again after pressing. This phenomenon plays the role of secondary support.

4.3. Analysis of steady thermal conduction properties

Fig. 12 shows the numerical analysis results gained by steady-state heat conduction of the bio-inspired structures. In the process of steady-state heat conduction, the re-entrant scapus structures show the best thermal conductivity, followed by the re-entrant double-crank structures, and the original bio-inspired structures have the worst thermal conductivity. The results show that during the steady heat conduction of the bio-inspired structures, the heat conduction temperature of the outer panel of PCS and DCS is 2.94 K and 0.81 K higher than that of CS. The thermal conductivity temperature of the outer wall of PHS and DHS is 11.62 K and 5.48 K higher than that of HS. The thermal conductivity temperature of the external wall of PPS and DPS is 4.6 K and −0.08 K higher than that of PS. In summary, the bio-inspired re-entrant components' design can improve the thermal conductivity of the traditional structures, and the re-entrant scapus structures can improve the heat dissipation capacity of the structures. It can be widely used in

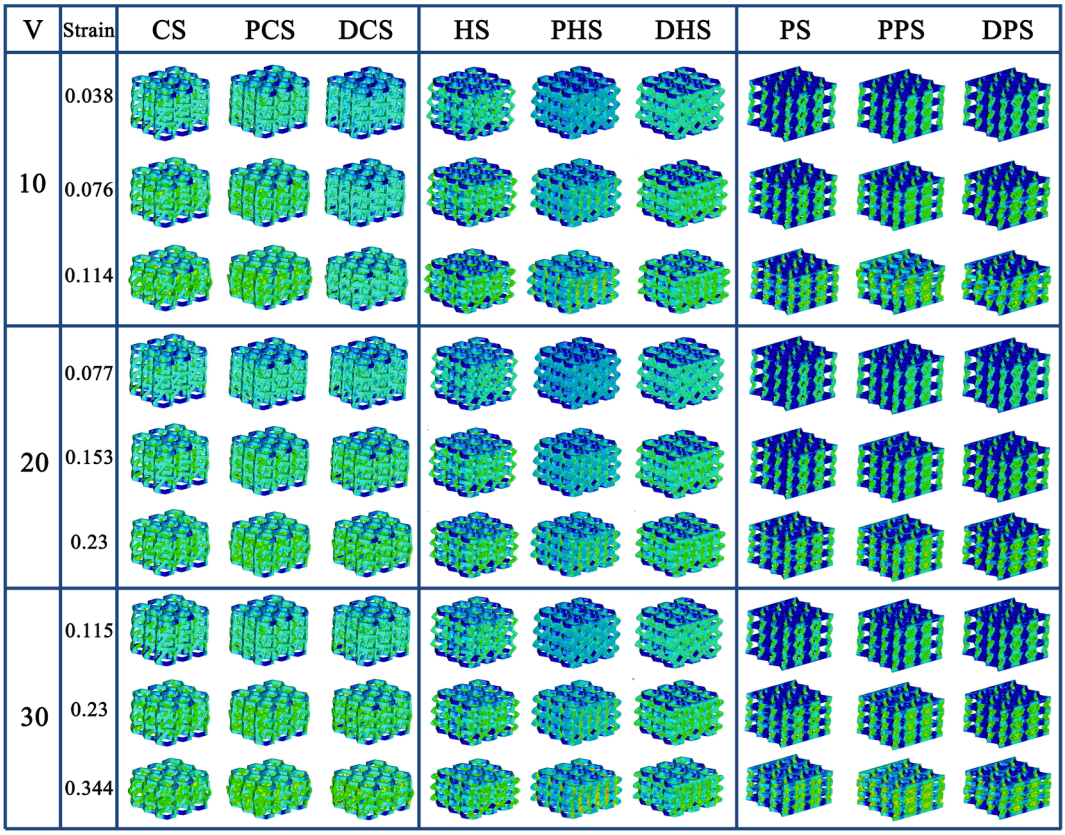

Fig. 11. Impact deformation modes of the bio-inspired structures.

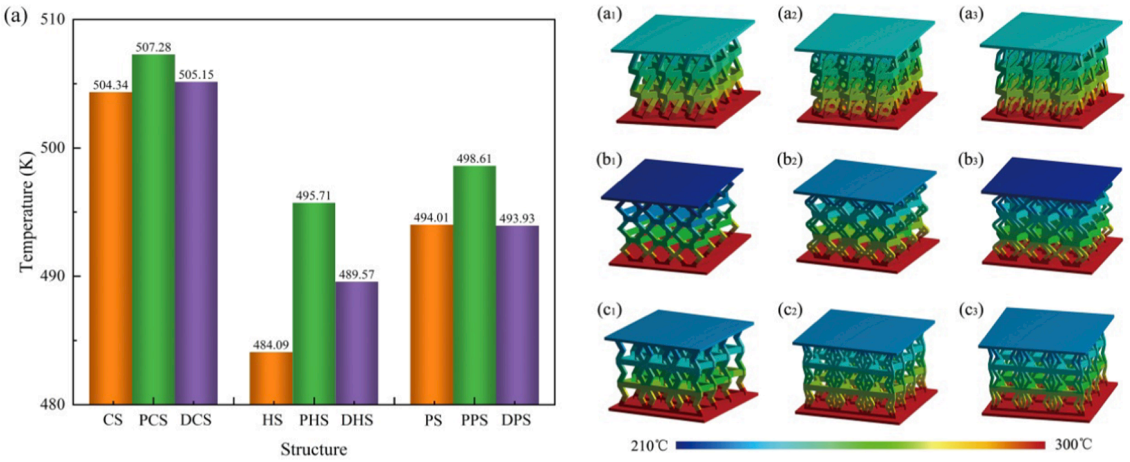

Fig. 12. Steady-state thermal conduction of the bio-inspired structures; (a) Temperature at the heat dissipation end of the bio-inspired structure; (b) steady-state heat conduction temperature distribution of the bio-inspired structures.

subsequent protection and heat dissipation engineering applications, such as heat conduction and protection of battery packaging.

5. Engineering applications

In the use of the electric-powered vehicle, the electric-powered vehicle hits nonfixed obstacles, and the obstacles then hit the bottom of the electric-powered vehicle, similar to the situation of the dynamic ball strike, as shown in Fig. 13 (A). The impact is likely to cause partial deformation of the battery pack bottom shell at the bottom of the electric-powered vehicle. In severe cases, the impact can even puncture the inner core of the battery pack and cause thermal runaway. At the same time, the development of the electric vehicle battery pack cooling system is also worth discussing. It is important to use the improved battery pack to dissipate the heat rapidly after the battery pack overheats, as shown in Fig. 13 (B). In this paper, the novel bio-inspired structure is used to improve the battery pack of electric-powered vehicles to achieve effective protection and proficient passive cooling of battery packs. Taking the ball-hit battery pack and the steady-state heat conduction after battery overheating as examples, the excellent characteristics of the improved battery pack are analyzed, as shown in Fig. 13.

When the bottom of the electric-powered vehicle is hit, the impact stress of the improved battery pack has even distribution due to the re-entrant lattice structure PCS. As can be seen from the stress nephogram shown in Fig. 14 ($a_{1\text{-}3}$, $b_{1\text{-}3}$), the stress distribution area of the improved battery pack becomes larger during the initial impact, and the impact energy is better dispersed. PCS absorbs the energy from the impact after the impact deformation, so the impact force is improved, as shown in Fig. 14 (A). When the battery pack is combined with the bio-inspired lattice structure PCS, the impact average load is increased, which improves the safety of the electric vehicle. Moreover, this is only the lifting

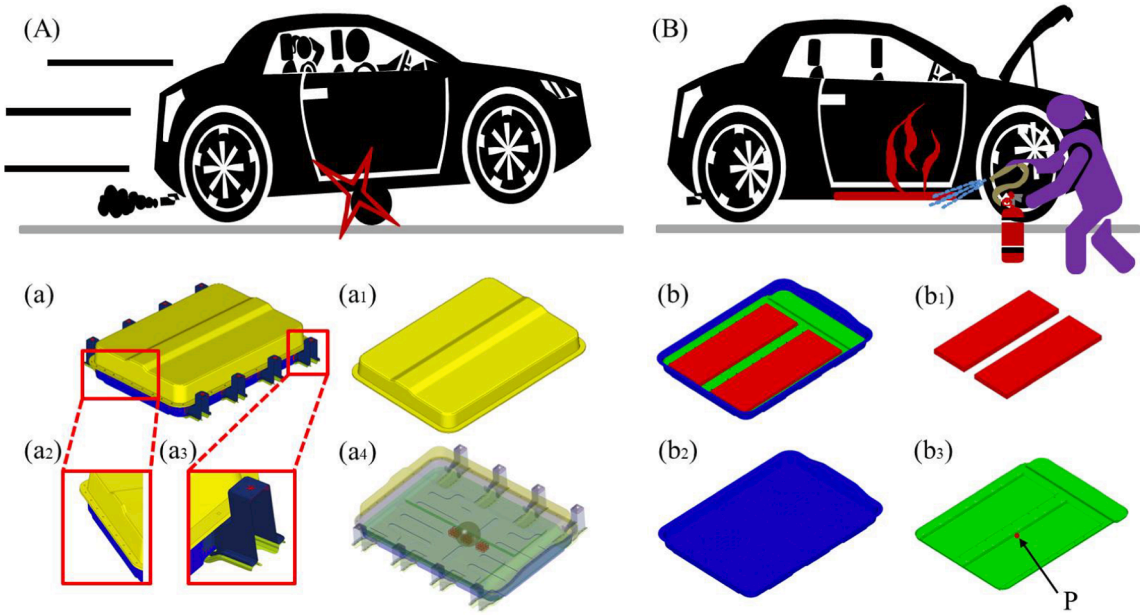

Fig. 13. The original and improved battery packs of the electric-powered vehicle; (A) The non-fixed obstacle hits the bottom of the electric-powered vehicle; (B) The battery pack overheating accident; (a) The battery pack model; (a_1) The top cover of the electric-powered car battery pack; (a_2) Finite element magnification of welding position of the electric-powered vehicle battery pack; (a_3) Rigid connection of the battery pack; (a_4) Ball hits improved battery pack model and the perspective view of the improved battery pack. The velocity of the ball is 5 m/s; (b) Inside view of the battery pack; (b_1) The simplified battery in the battery pack; (b_2) The bottom cover of the electric-powered battery pack; (b_3) The inner plate of the electric-powered battery pack. Point P is the temperature output point.

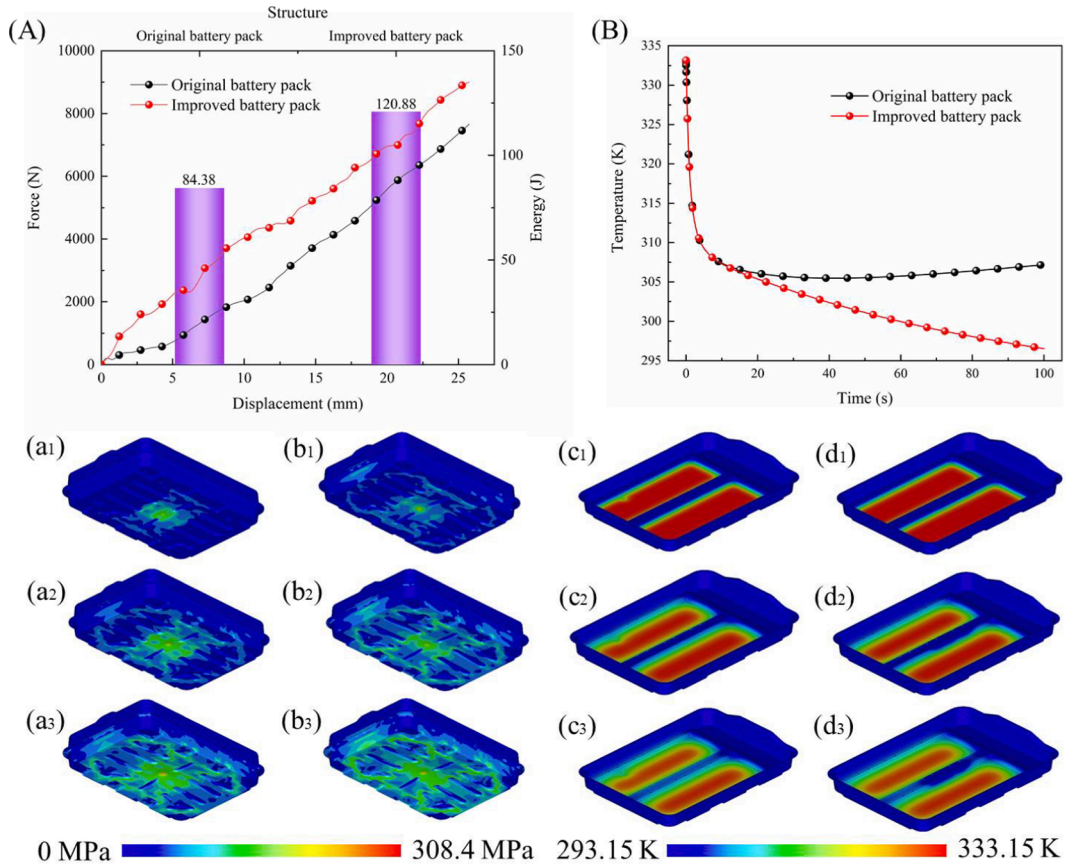

Fig. 14. The crashworthiness diagram of original and improved battery packs; (A) The thermal dissipation diagram of original and improved battery packs; (B) The crashworthiness diagram of original and improved battery packs; (a_1) The stress nephogram when the original battery pack is hit 7.75 mm; (a_2) The stress nephogram when the original battery pack is hit 15.25 mm; (a_3) The stress nephogram when the original battery pack is hit 22.75 mm; (b_1) The stress nephogram when the improved battery pack is hit 7.75 mm; (b_2) The stress nephogram when the improved battery pack is hit 15.25 mm; (b_3) The stress nephogram when the improved battery pack is hit 22.75 mm; (c_1) The temperature nephogram when the original battery pack dissipates heat for 20 s; (c_2) The temperature nephogram when the original battery pack dissipates heat for 66 s; (c_3) The temperature nephogram when the original battery pack dissipates heat for 100 s; (d_1) The temperature nephogram when the improved battery pack dissipates heat for 20 s; (d_2) The temperature nephogram when the improved battery pack dissipates heat for 66 s; (d_3) The temperature nephogram when the improved battery pack dissipates heat for 100 s.

protection effect of adding PCS to the impact site. It can be seen that the re-entrant improvement of the battery pack is extremely valuable to improve the safety of the electric-powered vehicle. In addition, the energy absorption comparison of original and improved battery packs shows that the impact energy absorption rate of the improved battery pack is increased to 43.26 % of the original, which is conducive to the improvement of the impact energy absorption performance.

When the battery in the battery pack rises sharply to 333.15 K, the electric-powered vehicle can stop in an emergency for heat dissipation. Considering the passive heat dissipation performance of the battery pack, the analysis results are shown in Fig. 14($c_{1\text{-}3}$, $d_{1\text{-}3}$). The improved battery pack can effectively improve the heat dissipation performance within the effective time, as shown in Fig. 14 (B). In the initial heat dissipation stage, the heat dissipation efficiency of original and improved battery packs is essentially the same due to the thermal radiation of the battery packs themselves. However, when the structural temperature reaches 307.5 K at the output point P, the temperature at the output point P of the original battery pack is unchanged in the following 90 s due to the high environmental temperature between the inner plate and the bottom cover. In contrast, the temperature of the output point P of the improved battery pack continues to drop due to the heat conduction effect of the bio-inspired structure. After the battery pack dissipates heat for 100 s, the temperature of the improved battery pack is 10.7 K lower than that of the original battery pack. This method efficiently improves the heat dissipation performance of the battery pack. In summary, the improved battery pack can efficiently improve the overall protection performance and heat dissipation performance of the battery pack structure, and this improvement method has extremely high engineering application value.

6. Conclusion

Based on the energy dissipation effect of gray crane feathers, structural assembly components are proposed. The assembled re-entrant structures undergo structural property tests, including compression, shock, and heat conduction tests. Through Euler theory analysis, the following conclusions are drawn:

(1) The re-entrant assembly provides secondary support during compression and bending deformation, significantly enhancing load-bearing characteristics and improving heat conduction properties.

(2) Euler theory accurately predicts the elastic modulus of complex structures, providing a theoretical basis for small deformation engineering applications.

(3) After improving the assembly of re-entrant components, the energy absorption rate of batteries in new energy vehicles increased by 143.26 %. Such improvements in re-entrant component assembly hold significant engineering application value.

CRediT authorship contribution statement

Ruiyao Liu: Writing – original draft, Writing – review & editing, Visualization, Project administration, Data curation, Formal analysis, Methodology, Software, Formal analysis. **Guofeng Yao:** Writing – review & editing, Visualization, Supervision, Conceptualization, Validation. **Jian Zhang:** Writing – review & editing. **Yanan Yang:** Writing – review & editing. **Zezhou Xu:** Writing – review & editing. **Yuting Liu:** Writing – review & editing. **Zhenglei Yu:** Writing – review & editing, Visualization, Funding acquisition, Resources, Conceptualization, Validation. **Liang ping:** Funding acquisition, Software, Validation. **Zhihui Zhang:** Writing – review & editing. **Lei Dong:** Software. **Chunyang Han:** Writing – review & editing.

Declaration of Competing Interest

The authors declare that they have no known competing financial interests or personal relationships that could have appeared to influence the work reported in this paper.

Data availability

Data will be made available on request.

Acknowledgments

This work is supported by National Key R&D program of China (2022YFB4600500), National Natural Science Foundation of China (No. 52375289), Science and Technology Development Program of Jilin Province, China (20230203031SF), National Natural Science Foundation of Chongqing (CSTB2022NSCQ-MSX0225), Capital construction funds within the budget of Jilin Provincial Development and Reform Commission (2023C041-4), The 5th Batch of Special Grants from China Postdoctoral Science Foundation (before the station) (2023TQ0129)).

Appendix A. Supplementary material

Supplementary data to this article can be found online at https://doi.org/10.1016/j.compstruct.2023.117599.

References

[1] Munch E, Launey M E, Alsem D H, et al. Tough, bio-inspired hybrid materials[J]. Science, 322.
[2] Fu K, Moreno D, Yang M, et al. Bio-inspired design: an overview investigating open questions from the broader field of design-by-analogy[J]. J Mech Des 2014;136 (11):111102.
[3] Douglas T. Materials science. A bright bio-inspired future[J]. Science 2003;299 (5610):1192–3.
[4] Djumas L, Molotnikov A, Simon GP, et al. Enhanced mechanical performance of bio-inspired hybrid structures utilising topological interlocking geometry[J]. Sci Rep 2016;6:26706.
[5] Bza B, Yl C, Jl C, et al. Novel mechanical behaviors of DNA-inspired helical structures with chirality[J]. Int J Mech Sci 2019;161–162:105025-.
[6] Yuan J, Cho SK. Bio-inspired micro/mini propulsion at air-water interface: a review [J]. J Mech Sci Technol 2012;26(12):3761–8.
[7] B h d a, b x j, b y w,, et al. Post-capture vibration suppression of spacecraft via a bio-inspired isolation system - ScienceDirect[J]. Mech Syst Sig Process 2018;105: 214–40.
[8] Zhang W, Yin S, Yu TX, et al. Crushing resistance and energy absorption of pomelo peel inspired hierarchical honeycomb[J]. Int J Impact Eng 2019;125(MAR.): 163–72.
[9] Bezazi A, Scarpa F, Remillat C. A novel centresymmetric honeycomb composite structure[J]. Compos Struct 2005;71(3/4):356–64.
[10] Lv WT, Dong L, Li D. A novel metamaterial with individually adjustable and sign-switchable Poisson's ratio[J]. Eur J Mech A Solids 2022;97:104851.
[11] Balawi S, Abot JL. A refined model for the effective in-plane elastic moduli of hexagonal honeycombs[J]. Compos Struct 2008;84(2):147–58.
[12] Wang Z, Zhang J, Li Z, et al. On the crashworthiness of bio-inspired hexagonal prismatic tubes under axial compression[J]. Int J Mech Sci 2020;186:105893.
[13] Pan J, Fang H, Xu MC, et al. Dynamic performance of a sandwich structure with honeycomb composite core for bridge pier protection from vehicle impact[J]. Thin-Walled Struct 2020;157(9):107010.
[14] Meran AP, Toprak T, MuAn A. Numerical and experimental study of crashworthiness parameters of honeycomb structures[J]. Thin-Walled Struct 2014; 78:87–94.
[15] Jrg Hohe A, Volker Hardenacke A, Valia Fascio B, et al. Numerical and experimental design of graded cellular sandwich cores for multi-functional aerospace applications- ScienceDirect[J]. Mater Des 2012;39:20–32.
[16] Mao A, Zhao N, Liang Y, et al. Mechanically Efficient Cellular Materials Inspired by Cuttlebone[J]. Adv Mater 2021;33(15):2007348.
[17] Sun M, Sun H, Hostler S, et al. Effects of feather-fiber reinforcement on poly(vinyl alcohol)/clay aerogels: structure, property and applications[J]. Polym.: Int. J. Sci. Technol. Polym. 2018.
[18] Gamble LL, Harvey C, Inman DJ. Load alleviation of feather-inspired compliant airfoils for instantaneous flow control[J]. Bioinspir Biomim 2020.
[19] Iwata M, Teshima M, Seki T, et al. Bio-inspired bright structurally colored colloidal amorphous array enhanced by controlling thickness and black background[J]. Adv Mater 2017;29(26):1605050.
[20] Sharma D, Hiremath SS. Engineering the failure path with bird feather inspired novel cellular structures[J]. Eng Fract Mech 2022;264:108350.
[21] Sharma D, Hiremath SS. Compressive and flexural properties of the novel lightweight tailored bio-inspired structures[J]. Thin-Walled Struct 2022;174: 109169.
[22] Lv WT, Li D, Dong L. Study on blast resistance of a composite sandwich panel with isotropic foam core with negative Poisson's ratio[J]. Int J Mech Sci 2021;191: 106105.
[23] Li D, Yin JH, Roderic DL, Lakes. Strong re-entrant cellular structures with negative Poisson's ratio[J]. J Mater Sci 2018;53(5):3493–9.
[24] Pelanconi M, Nature-Inspired OA. Ultra-lightweight structures with gyroid cores produced by additive manufacturing and reinforced by unidirectional carbon fiber ribs[J]. Materials 2019;12(24).
[25] Du Y, Gu D, Xi L, et al. Laser additive manufacturing of bio-inspired lattice structure: Forming quality, microstructure and energy absorption behavior[J]. Materials Science and Engineering, 2020, 773(Jan.31): 138857.1-138857.10.
[26] Pasquale G D, Luceri F. Experimental validation of Ti6Al4V bio-inspired cellular structures from additive manufacturing processes[J]. Mater Today: Proc 2019;7 (Part 1): 566-571.
[27] Saranathan V, Narayanan S, Sandy A, Dufresne ER, Prum RO. Evolution of single gyroid photonic crystals in bird feathers[J]. Proceedings of the National Academy of Sciences, 2021, 118(23): e2101357118.
[28] Guerra AJ, Ciurana J. 3D-printed bioabsordable polycaprolactone stent: The effect of process parameters on its physical features[J]. Mater Des 2017;137(jan.):430–7.
[29] Guo Y, Zhang J, Chen L, Du B, Liu Y. Deformation behaviors and energy absorption of auxetic lattice cylindrical structures under axial crushing load[J]. Aerosp Sci Technol 2020;98:105662.
[30] Liu S, Tong Z, Tang Z, Liu Y, Zhang Z. Bionic design modification of non-convex multi-corner thin-walled columns for improving energy absorption through adding bulkheads [J]. Thin Wall Struct 2015;88:70–81.
[31] Lee K, Yang Y, Kim S, Yang I. Energy absorption control characteristics of Al alloy thin-walled tubes under impact load [J]. Acta Mech Solida Sin 2008;21:383–8.
[32] Tan CY, Akil HM. Impact response of fiber metal laminate sandwich composite structure with polypropylene honeycomb core[J]. Compos B Eng 2012;43(3): 1433–8.
[33] Daryabeigi K. Heat Transfer in Adhesively Bonded Honeycomb Core Panels[J]. Journal of Thermophysics and Heat Transfer, 2002, 16(2): 217-217.
[34] Gibson L J. Cellular solids[J]. Mrs Bulletin, 2003, 28(4):110-111, 270-274.